JOURNAL OF SPACECRAFT AND ROCKETS
Vol. 31, No. 4, July–August 1994

Approximate Viscous Shock Layer Technique for Calculating Hypersonic Flows About Blunt-Nosed Bodies

F. McNeil Cheatwood*
ViGYAN, Inc., Hampton, Virginia 23665-0325
and
F. R. DeJarnette†
North Carolina State University Raleigh, North Carolina 27695-7910

An axisymmetric approximate method has been developed which can reliably calculate laminar (perfect gas, nonequilibrium, equilibrium) and turbulent (perfect gas and equilibrium) viscous hypersonic flows over blunt-nosed bodies. By substituting Maslen's second-order pressure expression for the normal momentum equation, a simplified form of the viscous shock layer (VSL) equations is obtained. Unlike other VSL solvers, this approach can solve both the subsonic and supersonic regions of the shock layer without a starting solution for the shock shape. The procedure is significantly faster than the parabolized Navier-Stokes and VSL solvers and would be useful in a preliminary design environment. It could also be used to provide a flowfield initialization for higher order procedures. Solutions have been generated for air flows over analytic body shapes. Surface heat transfer and pressure predictions are generally in very good agreement with VSL results. In addition, computed heating rates are in good agreement with experimental data.

Nomenclature

C_p = specific heat at constant pressure
c_i = mass fraction of species i
h = static enthalpy
h_1, h_3 = metrics (shape factors) of coordinate system
$\mathcal{J}_i$ = diffusion mass flux of species i
k = thermal conductivity
Le_{12} = binary Lewis number
M = Mach number
$\mathcal{M}$ = molecular weight
N_s = number of reacting species
n = normal distance from the shock
Pr = Prandtl number, $\mu C_p / k$
p = pressure
q = heat transfer rate
R = radius of curvature
Re = Reynolds number, $\rho u R_{\text{nose}} / \mu$
$\mathcal{R}$ = specific gas constant, $\mathcal{R}_u / \mathcal{M}$
$\mathcal{R}_u$ = universal gas constant
r = radius measured from axis of symmetry
s = distance measured along the shock wave
s_b = distance measured along the body surface
T = temperature
u = velocity component tangent to the shock wave
V = total velocity; $V^2 = u^2 + v^2$
v = velocity component normal to the shock wave
$\dot{w}_i$ = mass rate of formation of species i
Z = compressibility factor (equilibrium flow)
z = axial distance, measured from shock origin
Γ = angle measured relative to body axis
ϵ = Reynolds number parameter, $\epsilon^2 = \mu^*_{\text{ref}} / (\rho^*_\infty u^*_\infty R^*_{\text{nose}})$
ϵ^+ = eddy viscosity ratio, μ_t / μ
η = stream function ratio, ψ / ψ_s
η_n = computational n coordinate, $1 - n / n_b$
κ = curvature, $1 / R$
μ = dynamic viscosity
ξ = computational s coordinate, s
ρ = density
ψ = stream function

Superscripts

$\bar{}$ = normalized by shock value at current station
$*$ = dimensional quantity

Subscripts

b = body value
f = chemically frozen value
i = value for species i
j = denotes jth point within shock layer
nose = nose value
ref = reference condition
s = shock value
t = turbulent value
w = Wall value
0 = stagnation line value ($\xi = 0$)
∞ = freestream condition

Received Nov. 14, 1992; revision received May 19, 1993; accepted for publication May 21, 1993.

*Research Engineer. Member AIAA.
†Professor, Mechanical and Aerospace Engineering Department. Associate Fellow AIAA.

Introduction

ONGOING investigations into configurations such as the Aeroassist Space Transfer Vehicle (ASTV), the National Aero-Space Plane (NASP), and the Personnel Launch System (PLS), with their associated high-altitude, high-speed environments, have sparked renewed interest in hypersonic aerodynamics.[1] Particular attention has been focused on the use of numerical methods for flowfield predictions. Since excessive computer run times prevent benchmark approaches from being used in the preliminary design environment, there is a continued interest in developing improved engineering methods.

Accurate predictions of the flowfield properties may be obtained from solutions to the Navier-Stokes,[2] the parabolized Navier-Stokes,[3-5] or the viscous shock layer[6-9] equations. The full Navier-Stokes equations are typically solved using a time-marching procedure in order to properly model their elliptic behavior (a very costly computation). The parabolized Navier-

Stokes (PNS) and viscous shock layer (VSL) equations are derived from the steady, compressible Navier-Stokes equations. Both equation sets have been parabolized in the streamwise direction so that a solution may be advanced downstream using spatial marching techniques. Unfortunately, the computational requirements of existing methods for solving these equations exceed that which can be tolerated in preliminary parametric design studies.

Grantz et al.[10] employ the second-order Maslen pressure relation,[11] along with a simple linear expression for the normal component of velocity, in an approximate VSL approach. Boundary-layer-like viscous terms are added to the inviscid streamwise momentum and energy equations to obtain a parabolic equation set similar to the full VSL equations. Since the shock shape is part of the solution, no initial shock shape or smoothing of intermediate shock shapes (both required for the VSL technique) is necessary. The technique is applicable to perfect gas and equilibrium flows.

This paper describes another approach which employs Maslen's pressure relation in lieu of the normal momentum equation. However, unlike Ref. 10, the remaining fluid equations are identical to the full VSL equations. This algorithm solves the equations in a shock-normal coordinate system and was originally presented in Refs. 12–14. The technique is applicable to perfect gas, equilibrium, and nonequilibrium flows. Comparisons between the results of the current approach, the method of Ref. 10 (for perfect gas flows), and a full VSL solver[8,15,16] are presented for analytic body shapes. Also, comparisons with experimental data[17,18] are made.

Analysis

In the analysis below, a brief discussion of the development of the governing equations is given. The boundary conditions, thermodynamic and transport properties, and the limiting forms of the governing equations are also discussed. In addition, key differences between the current approach and Ref. 10 are cited.

Governing Equations

The current approach starts with the full VSL equations written in orthogonal curvilinear coordinates. As mentioned earlier, only axisymmetric flow is considered. The equations are cast in a shock-normal (rather than the traditional body-normal) coordinate system, as illustrated in Fig. 1. This step is necessary to facilitate the use of Maslen's pressure relation which replaces the normal momentum equation. Since the remaining equations are unchanged, the normal component of velocity is found by solving the continuity equation rather than assuming a profile as was done in Ref. 10. If the form of the energy and streamwise momentum equations used in Ref. 10 is compared to the full VSL equations in the shock-normal system, it can be noted that several higher order terms (involving the variation of the metrics across the shock layer) have been neglected. These higher order terms are retained in the present approach.

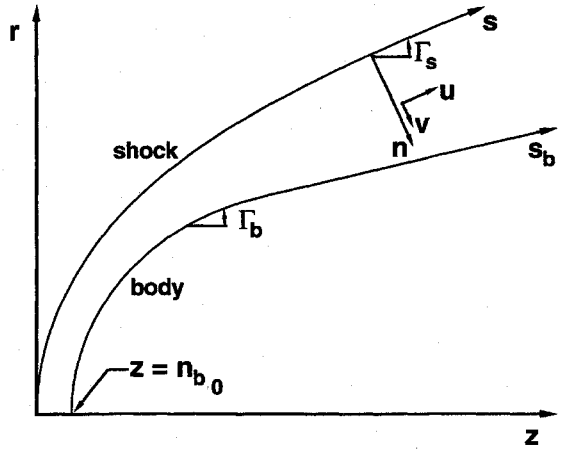

Fig. 1 Shock-oriented coordinate system.

The VSL equations[6] for axisymmetric flow, written in curvilinear coordinates, are presented below (excluding the normal momentum equation) in nondimensional form for

1) Continuity:

$$\frac{\partial}{\partial s}(\rho u h_3) + \frac{\partial}{\partial n}(\rho v h_1 h_3) = 0 \tag{1}$$

2) The s-momentum:

$$\rho\left(\frac{u}{h_1}\frac{\partial u}{\partial s} + v\frac{\partial u}{\partial n} + \frac{uv}{h_1}\frac{\partial h_1}{\partial n}\right) + \frac{1}{h_1}\frac{\partial p}{\partial s}$$
$$= \epsilon^2\left\{\frac{\partial}{\partial n}\left[\mu\left(1+\epsilon^+\right)\frac{\partial u}{\partial n} - \mu\frac{u}{h^1}\frac{\partial h_1}{\partial n}\right]\right.$$
$$\left. + \left(\frac{2}{h_1}\frac{\partial h_1}{\partial n} + \frac{1}{h_3}\frac{\partial h_3}{\partial n}\right)\left[\mu\left(1+\epsilon^+\right)\frac{\partial u}{\partial n} - \mu\frac{u}{h_1}\frac{\partial h_1}{\partial n\mathrm{M}}\right]\right\} \tag{2}$$

3) Energy:

$$\rho\left(\frac{u}{h_1}\frac{\partial h}{\partial s} + v\frac{\partial h}{\partial n}\right) - \frac{u}{h_1}\frac{\partial p}{\partial s} - v\frac{\partial p}{\partial n}$$
$$= \epsilon^2\left\{\frac{\partial}{\partial n}\left[\frac{\mu}{Pr}\left(1+\epsilon^+\frac{Pr}{Pr_t}\right)\frac{\partial h}{\partial n}\right]\right.$$
$$+ \frac{\mu}{Pr}\left(1+\epsilon^+\frac{Pr}{Pr_t}\right)\frac{\partial h}{\partial n}\left(\frac{1}{h_1}\frac{\partial h_1}{\partial n} + \frac{1}{h_3}\frac{\partial h_3}{\partial n}\right)$$
$$\left. + \mu\left(1+\epsilon^+\right)\left[\left(\frac{\partial u}{\partial n}\right)^2 - 2\frac{u}{h_1}\frac{\partial h_1}{\partial n}\frac{\partial u}{\partial n}\right] + \mu\left(\frac{u}{h_1}\frac{\partial h_1}{\partial n}\right)^2\right\} \tag{3}$$

These equations, which are applicable to perfect gas and equilibrium flowfields, use an eddy-viscosity model to accommodate turbulent flow calculations (for laminar flow, $\epsilon^+ = 0$). Currently, the Cebeci-Smith algebraic eddy-viscosity model[19] is employed.

In nonequilibrium flows, the characteristic time scales of the chemical reactions are of the same order as the time scales of the mean flow. The continuity and streamwise momentum equations given above (with $\epsilon^+ = 0$) are still valid for these flows. However, it is advantageous to recast the energy equation in terms of temperature:

$$\rho C_{pf}\left(\frac{u}{h_1}\frac{\partial T}{\partial s} + v\frac{\partial T}{\partial n}\right) - \frac{u}{h_1}\frac{\partial p}{\partial s} - v\frac{\partial p}{\partial n}$$
$$= \epsilon^2\left\{\frac{\partial}{\partial n}\left[k\frac{\partial T}{\partial n}\right] + k\frac{\partial T}{\partial n}\left(\frac{1}{h_1}\frac{\partial h_1}{\partial n} + \frac{1}{h_3}\frac{\partial h_3}{\partial n}\right)\right.$$
$$\left. + \mu\left(\frac{\partial u}{\partial n} - \frac{u}{h_1}\frac{\partial h_1}{\partial n}\right)^2\right\} - \epsilon^2\sum_{i=1}^{N_s}\mathcal{J}_i C_{p_i}\frac{\partial T}{\partial n} - \sum_{i=1}^{N_s} h_i \dot{w}_i \tag{4}$$

In addition, the species conservation equations must be solved to determine the local composition of the fluid:

$$\rho\left(\frac{u}{h_1}\frac{\partial c_i}{\partial s} + v\frac{c_i}{\partial n}\right) = \dot{w}_i$$
$$- \epsilon^2\left\{\frac{\partial \mathcal{J}_i}{\partial n} + \mathcal{J}_i\left(\frac{1}{h_1}\frac{\partial h_1}{\partial n} + \frac{1}{h_3}\frac{\partial h_3}{\partial n}\right)\right\} \tag{5}$$

The subscript i is the species index. Table 1 provides an indexing key for the seven-species air model[20] used here, while Table 2 lists the reactions and catalytic third bodies (M_r) which are considered.

Several terms which were absent in the perfect gas and equilibrium analysis are present here. First, $\dot{w}_i$ is the species rate of production term. This source term is a function of both T and c_i. The binary diffusion mass flux is

$$\mathcal{J}_i = -\frac{k}{C_{pf}} Le_{12} \frac{\partial c_i}{\partial n}$$

where Le_{12} is the binary Lewis number ($Le_{12} = 1.4$ is used here). The species' mass fractions are

$$c_i = \frac{\rho_i}{\rho}$$

where

$$\sum_{i=1}^{N_s} c_i = 1$$

The above expressions are written in nondimensional form. A partial list of the definitions of these nondimensional quantities is given here (see Ref. 13 for the complete set):

$$s = \frac{s^*}{R^*_{\text{nose}}} \qquad n = \frac{n^*}{R^*_{\text{nose}}} \qquad p = \frac{p^*}{p^*_{\text{ref}}}$$

$$u = \frac{u^*}{V^*_\infty} \qquad v = \frac{v^*}{V^*_\infty} \qquad \rho = \frac{\rho^*}{\rho^*_\infty}$$

$$h = \frac{h^*}{h^*_{\text{ref}}} \qquad q = \frac{q^*}{q^*_{\text{ref}}} \qquad \mu = \frac{\mu^*}{\mu^*_{\text{ref}}}$$

$$k = \frac{k^*}{k^*_{\text{ref}}} \qquad \dot{w}_i = \frac{\dot{w}_i^*}{\dot{w}^*_{\text{ref}}} \qquad T = \frac{T^*}{T^*_{\text{ref}}}$$

where the reference quantities are

$$p^*_{\text{ref}} = \rho^*_\infty V^{*2}_\infty \qquad h^*_{\text{ref}} = V^{*2}_\infty \qquad q^*_{\text{ref}} = \rho^*_\infty V^{*3}_\infty$$

$$k^*_{\text{ref}} = \mu^*_{\text{ref}} C^*_{p\infty} \qquad \dot{w}^*_{\text{ref}} = \frac{\rho^*_\infty V^*_\infty}{R^*_{\text{nose}}} \qquad T^*_{\text{ref}} = \frac{V^{*2}_\infty}{C^*_{p\infty}}$$

and μ^*_{ref} is the coefficient of viscosity evaluated at T^*_{ref}.

This equation set could be transformed to either a body-normal or shock-normal system, since the metrics have been left arbitrary to this point. For the shock-oriented coordinate system employed here, the metrics are

$$h_1 = 1 - n\kappa_s \qquad h_3 = r = r_s - n\cos\Gamma_s$$

where n is the inward normal distance from the shock and κ_s is the shock curvature (see Fig. 1). To facilitate the solution of the governing equations, a transformation to normalized coordinates is performed:

$$\xi = s \qquad \eta_n = 1 - \frac{n}{n_b}$$

$$\bar{u} = \frac{u}{u_s} \qquad \bar{\rho} = \frac{\rho}{\rho_s}$$

where n_b and the shock properties are functions of ξ only. Note that $\eta_n = 0$ on the body and $\eta_n = 1$ at the shock. In this coordinate system, the derivatives are

$$\frac{\partial}{\partial s} = \frac{\partial}{\partial \xi} - \frac{(\eta_n - 1)}{n_b}\frac{dn_b}{d\xi}\frac{\partial}{\partial \eta_n} \qquad \frac{\partial}{\partial n} = -\frac{1}{n_b}\frac{\partial}{\partial \eta_n}$$

The governing equations in this transformed system are given below for

1) Continuity:

$$\frac{\partial}{\partial \xi}(\rho_s \bar{\rho} u_s \bar{u} h_3) - \rho_s u_s \frac{\eta_n - 1}{n_b}\frac{dn_b}{d\xi}\frac{\partial}{\partial \eta_n}(\bar{\rho}\bar{u}h_3) - \frac{\rho_s}{n_b}\frac{\partial}{\partial \eta_n}(\bar{\rho} v h_1 h_3) = 0 \tag{6}$$

2) The ξ-momentum:

$$\rho_s\bar{\rho}\left(\frac{\bar{u}}{h_1}\left[u_s\frac{\partial \bar{u}}{\partial \xi} + \bar{u}\frac{du_s}{d\xi} - u_s\frac{\eta_n - 1}{n_b}\frac{dn_b}{d\xi}\frac{\partial \bar{u}}{\partial \eta_n}\right] - \frac{v}{n_b}\left[\frac{\partial \bar{u}}{\partial \eta_n} + \frac{\bar{u}}{h_1}\frac{\partial h_1}{\partial \eta_n}\right]\right) + \frac{1}{h_1 u_s}\left[\frac{\partial p}{\partial \xi} - \frac{\eta_n - 1}{n_b}\frac{dn_b}{d\xi}\frac{\partial p}{\partial \eta_n}\right]$$
$$= \frac{\epsilon^2}{n_b^2}\left\{\frac{\partial}{\partial \eta_n}\left[\mu\left(\frac{\partial \bar{u}}{\partial \eta_n} - \frac{\bar{u}}{h_1}\frac{\partial h_1}{\partial \eta_n}\right)\right] + \mu\left(\frac{2}{h_1}\frac{\partial h_1}{\partial \eta_n} + \frac{1}{h_3}\frac{\partial h_3}{\partial \eta_n}\right)\left(\frac{\partial \bar{u}}{\partial \eta_n} - \frac{\bar{u}}{h_1}\frac{\partial h_1}{\partial \eta_n}\right)\right\} \tag{7}$$

3) Energy:

$$\rho_s\bar{\rho}\left(\frac{u_s\bar{u}}{h_1}\left[\frac{\partial h}{\partial \xi} - \frac{\eta_n - 1}{n_b}\frac{dn_b}{d\xi}\frac{\partial h}{\partial \eta_n}\right] - \frac{v}{n_b}\frac{\partial h}{\partial \eta_n}\right) - \frac{u_s\bar{u}}{h_1}\left[\frac{\partial p}{\partial \xi} - \frac{\eta_n - 1}{n_b}\frac{dn_b}{d\xi}\frac{\partial p}{\partial \eta_n}\right] + \frac{v}{n_b}\frac{\partial p}{\partial \eta_n}$$
$$= \frac{\epsilon^2}{n_b^2}\left\{\frac{\partial}{\partial \eta_n}\left[\frac{\mu}{Pr}\frac{\partial h}{\partial \eta_n}\right] + \frac{\mu}{Pr}\frac{\partial h}{\partial \eta_n}\left(\frac{1}{h_1}\frac{\partial h_1}{\partial \eta_n} + \frac{1}{h_3}\frac{\partial h_3}{\partial \eta_n}\right) + u_s^2\mu\left(\frac{\partial \bar{u}}{\partial \eta_n} - \frac{\bar{u}}{h_1}\frac{\partial h_1}{\partial \eta_n}\right)^2\right\} \tag{8}$$

Table 1 Species indexing

i	1	2	3	4	5	6	7
Species	N_2	O_2	N	O	NO	NO^+	e^-

Table 2 Chemical reactions

r	Reaction	M_r
1	$O_2 + M_1 \rightleftarrows 2O + M_1$	N_2, O_2, O, NO, N
2	$N_2 + M_2 \rightleftarrows 2N + M_2$	N_2, O_2, O, NO
3	$N_2 + M_3 \rightleftarrows 2N + M_3$	N
4	$NO + M_4 \rightleftarrows N + O + M_4$	N_2, O_2, O, NO, N
5	$NO + O \rightleftarrows O_2 + N$	
6	$N_2 + O \rightleftarrows NO + N$	
7	$N + O \rightleftarrows NO^+ + e^-$	

4) energy (nonequilibrium):

$$\rho_s\bar{\rho}C_{pf}\left(\frac{u_s\bar{u}}{h_1}\left[\frac{\partial T}{\partial\xi}-\frac{\eta_n-1}{n_b}\frac{dn_b}{d\xi}\frac{\partial T}{\partial\eta_n}\right]-\frac{v}{n_b}\frac{\partial T}{\partial\eta_n}\right)$$
$$-\frac{u_s\bar{u}}{h_1}\left[\frac{\partial p}{\partial\xi}-\frac{\eta_n-1}{n_b}\frac{dn_b}{d\xi}\frac{\partial p}{\partial\eta_n}\right]+\frac{v}{n_b}\frac{\partial p}{\partial\eta_n}$$
$$=-\sum_{i=1}^{N_s}h_i\dot{w}_i\frac{\epsilon^2}{n_b^2}\left\{\frac{\partial}{\partial\eta_n}\left[k\frac{\partial T}{\partial\eta_n}\right]+k\frac{\partial T}{\partial\eta_n}\left(\frac{1}{h_1}\frac{\partial h_1}{\partial\eta_n}+\frac{1}{h_3}\frac{\partial h_3}{\partial\eta_n}\right)\right.$$
$$\left.+u_s^2\,\mu\left(\frac{\partial\bar{u}}{\partial\eta_n}-\frac{\bar{u}}{h_1}\frac{\partial h_1}{\partial\eta_n}\right)^2\right\}+\frac{\epsilon^2}{n_b}\sum_{i=1}^{N_s}\mathcal{J}_iC_{p_i}\frac{\partial T}{\partial\eta_n} \quad (9)$$

5) species conservation:

$$\rho_s\bar{\rho}\left(\frac{u_s\bar{u}}{h_1}\left[\frac{\partial c_i}{\partial\xi}-\frac{\eta_n-1}{n_b}\frac{dn_b}{d\xi}\frac{\partial c_i}{\partial\eta_n}\right]-\frac{v}{n_b}\frac{\partial c_i}{\partial\eta_n}\right)$$
$$=\dot{w}_i+\frac{\epsilon^2}{n_b}\left\{\frac{\partial\mathcal{J}_i}{\partial\eta_n}+\mathcal{J}_i\left(\frac{1}{h_1}\frac{\partial h_1}{\partial\eta_n}+\frac{1}{h_3}\frac{\partial h_3}{\partial\eta_n}\right)\right\} \quad (10)$$

In the approximate VSL method, Maslen's second-order pressure equation is used in lieu of numerically integrating the n-momentum equation:

$$p=p_s+\frac{\kappa_s r_s u_s}{2}(\eta-1)$$
$$-\frac{v_s\sin\Gamma_s}{4}\left[1+\frac{\kappa_s r_s}{u_s}\right](\eta^2-1) \quad (11)$$

where $\eta=\psi/\psi_s$ and ψ is the stream function. This explicit relation offers an attractive alternative to numerically integrating the normal momentum equation to solve for p, since it expresses p simply as a function of the shock properties at the current station and η. The variable η should not be confused with the transformation variable η_n defined previously. The relationship between these distinct quantities (which is derived from the continuity equation) is given below:

$$\psi_s\eta=n_b^2\left[\rho_s u_s^2\int_0^{\eta_n}\bar{\rho}\bar{u}\,(\eta_n-1)\,d\eta_n\right]$$
$$+n_b\left[\rho_s u_s r_s\int_0^{\eta_n}\bar{\rho}\bar{u}d\eta_n\right] \quad (12)$$

The above set of equations is supplemented by the equation of state. For equilibrium air,

$$p=\rho Z\mathcal{R}_{\text{air}}T \quad (13)$$

where $Z=1$ for perfect gas flows. For nonequilibrium flows, air is modeled as a mixture of thermally perfect gases, so the perfect gas equation of state is still valid. However, the mixture molecular weight ($\mathcal{M}$) is variable, so that the equation of state is

$$p=\rho\frac{\mathcal{R}_u}{\mathcal{M}}T \quad (14)$$

where

$$\mathcal{M}=\left(\sum_{i=1}^{N_s}\frac{c_i}{\mathcal{M}_i}\right)^{-1}$$

Thermodynamic and Transport Properties

For perfect gas flows, the specific heat is constant. In addition, Sutherland's law is employed to calculate the viscosity, while the Prandtl number is assumed to be $Pr=0.72$ throughout the shock layer.

Hansen's model[21] is used to define thermodynamic and transport properties (Z, μ, and Pr) for the equilibrium flow solutions presented in this paper. The relations for these variables are used to generate a table of data which spans a large range of values for p, h, and T. These tabulated values are then interpolated as needed during the numerical solution of the governing equations.

In nonequilibrium flows, the thermodynamic and transport properties are required for each species present in the fluid. Expressions from Ref. 22 are used to define C_{p_i}, h_i, μ_i, and k_i. The thermodynamic properties for the gas mixture are

$$h=\sum_{i=1}^{N_s}c_ih_i$$

and

$$C_{pf}=\sum_{i=1}^{N_s}c_iC_{p_i}$$

The transport properties are governed by more complicated mixing laws. Currently, the methods of Armaly and Sutton[23] and Mason and Saxena[24] are used to define the mixture viscosity and mixture conductivity, respectively.

Boundary Conditions

The no-slip condition ($u_w=v_w=0$) is applied at the wall. In addition, the wall temperature, which can be variable, must be specified. Further, for nonequilibrium flows, boundary conditions must be supplied for the species continuity equations. Currently, the options are for the surface to be either fully catalytic or noncatalytic.

The shock jump conditions are given by the Rankine-Hugoniot relations. For perfect gas flow, these are closed-form expressions. However, these equations must be solved in an iterative fashion for equilibrium and nonequilibrium flow. For all flow regimes, the derivatives of u_s, p_s, and v_s with respect to ξ are also required.

Stagnation Line Solution

The stagnation line is a singularity in the standard VSL equations. Typically, this singularity is handled by expanding the dependent variables on the stagnation line in power series of ξ. Usually, these expressions are truncated to include no more than the second-order terms. This approach reduces the governing partial differential equations to ordinary differential equations on the stagnation line.

In the shock-oriented system used here, an explicit limiting form of the governing equations as $\xi\to 0$ can be calculated. This approach yields a set of ordinary differential equations which is consistent with the general governing equations (see Refs. 12–14). With the form of the streamwise momentum equation used in Ref. 10, a correction term had to be carried along throughout the shock layer to force the solution to smoothly approach its stagnation value. Despite these efforts, the stagnation solution was not consistent with the remainder of the layer. In the current research, no such correction term was required and the problem with the limiting form of the equations as they near the stagnation line has been successfully addressed.

Method of Solution

Equations of Standard Parabolic Form

The streamwise momentum, energy, and species conservation equations (which are nonlinear) can be cast in the following

standard form for parabolic partial differential equations:

$$A_0\frac{\partial^2 W}{\partial \eta_n^2} + A_1\frac{\partial W}{\partial \eta_n} + A_2 W + A_3 + A_4\frac{\partial W}{\partial \xi} = 0 \qquad (15)$$

where the scalar W represents the dependent variables $\bar{u}$, h, T, and c_i, respectively, and the coefficients A_0, A_1, A_2, A_3, A_4 may be determined from Eqs. (7–10). For the energy and species conservation equations, the nonlinearities are handled through a simple lagging technique. However, to speed convergence, the streamwise momentum equation is quasilinearized (see Ref. 13 for details).

In the finite-difference representations of the partial differential equations, a two-point backward difference is used for the derivatives with respect to ξ. Since this is a fully implicit scheme, three-point central differencing of values at the current station is used for the partial derivatives with respect to η_n. Evaluating the coefficients of the resulting finite-difference expression at discrete points across the shock layer yields a tridiagonal system of equations which is solved using Thomas' algorithm.

Advancing the Solution

The shock shape is required to solve the governing equations. The full VSL approach requires the user to input an initial shock shape, which is used to calculate a first iteration solution for the entire flow domain. The shock shape calculated in this pass must then be smoothed and used as the input shape for a second iteration. This process is continued until the new calculated shock shape varies little from the input shape (usually two or three iterations). In the design environment, such requirements of the user are undesirable.

This issue is addressed in Ref. 10 by incorporating a shock iteration technique in the solution. Since the subsonic-transonic region is elliptic in nature, this portion of the flowfield must be solved in a global fashion. The derivative of shock layer thickness is described in terms of a cubic equation involving the body radius where an iterative procedure is applied to determine its coefficients. This process typically requires 10–20 iterations to obtain a converged shock shape. A marching technique is employed aft of the subsonic-transonic region, since the inviscid layer is supersonic. For this region, the shock shape at the current station is extrapolated from the previous station using a cubic equation for the shock radius as a function of axial location. Requirements that this expression match the position, slope, and curvature at the previous station leaves one free coefficient (essentially the shock curvature derivative). An iterative technique is employed to determine its value, and then the solution is advanced downstream to the next station. The iterative procedure used in Ref. 10 is fairly sensitive, so this marching technique is often slow to converge.

The current approach parallels that of Ref. 10 in that the shock shape is generated as part of the solution, rather than being a required user input. Riley and DeJarnette[25] developed an algorithm which provides a smooth shock shape with relatively few iterations. Their approach serves as a model for the technique employed here. First, freestream properties are used to define initial profiles along the stagnation line. For the subsonic region, a conic equation is used to describe the shock radius as a function of axial position. The values of its two coefficients are determined through a quasi-Newton iterative procedure. Typically only four to six iterations are required to converge the shock shape. The marching procedure again utilizes a cubic equation with one parameter to be determined iteratively using the secant method. However, the iteration involves the shock curvature (rather than its derivative as in Ref. 10) which proves to be a much less sensitive parameter. As a result, convergence is typically achieved with three to four iterations per station.

Results and Discussion

In an effort to evaluate the accuracy of this new approach, a variety of test cases were run. For perfect gas flows, comparisons are made between the results of the VSL,[15] Grantz et al.,[10] and present approaches. For equilibrium flows, comparisons are made between the VSL[8] and present approaches. For nonequilibrium flows, comparisons between the VSL[16] and present methods are made. The above results are shown in conjunction with experimental[17,18] values where available. Note that the results are plotted in nondimensional form.

Perfect Gas

As a first case, the Mach 10.6 flow over a 15-deg sphere-cone is calculated. The nose radius is $R^*_{nose} = 0.375$ in. and the solution is computed for a body length of $s_{b_{end}} = 50$. The freestream conditions are $p^*_\infty = 0.01915$ psi and $T^*_\infty = 85°R$, with a wall temperature of $T^*_w = 540°R$. In Fig. 2, the heating results from the three solutions are presented and are seen to compare well (generally within 15%) with Cleary's experimental data.[17] Figure 3 provides more detailed information on the stagnation region and shows that the heating results from the current method approach the stagnation line value more smoothly than those from the other two methods. The computed

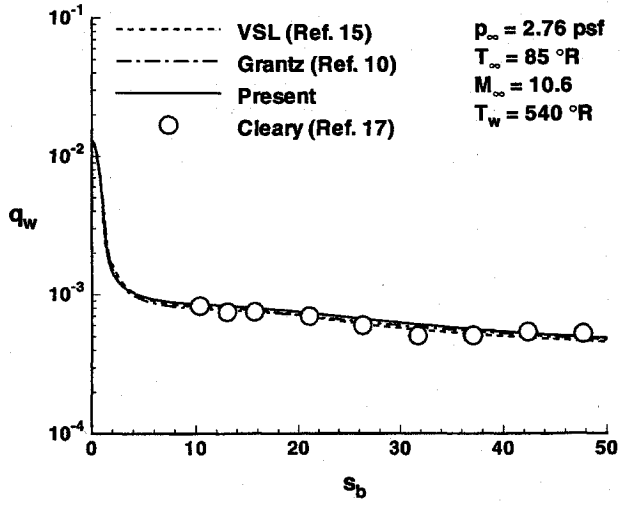

Fig. 2 Heat transfer comparison for 15-deg sphere-cone, R^*_{nose} = 0.375 in.

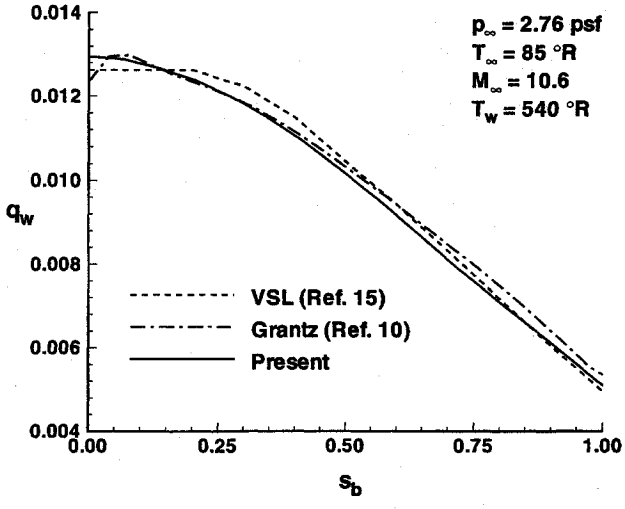

Fig. 3 Heat transfer comparison for 15-deg sphere-cone, R^*_{nose} = 0.375 in. (stagnation region).

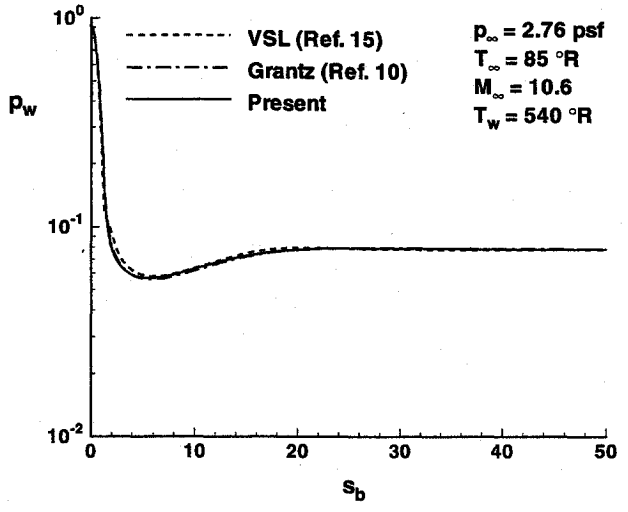

Fig. 4 Body pressure comparison for 15-deg sphere-cone, R^*_{nose} = 0.375 in.

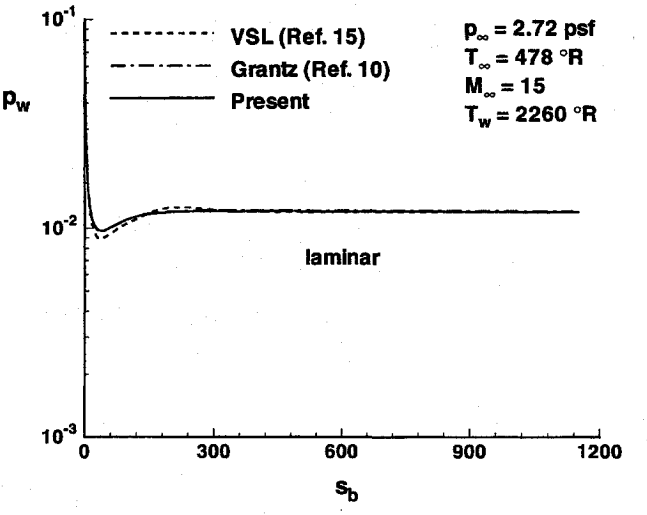

Fig. 6 Body pressure comparison for 5-deg sphere-cone, R^*_{nose} = 1.5 in.

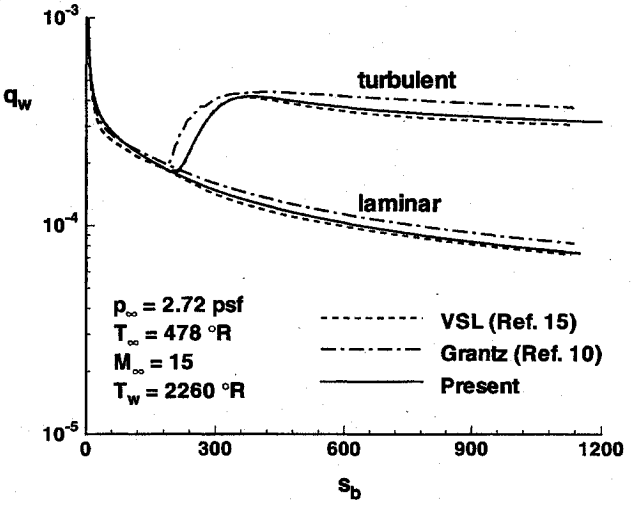

Fig. 5 Heat transfer comparison for 5-deg sphere-cone, R^*_{nose} = 1.5 in.

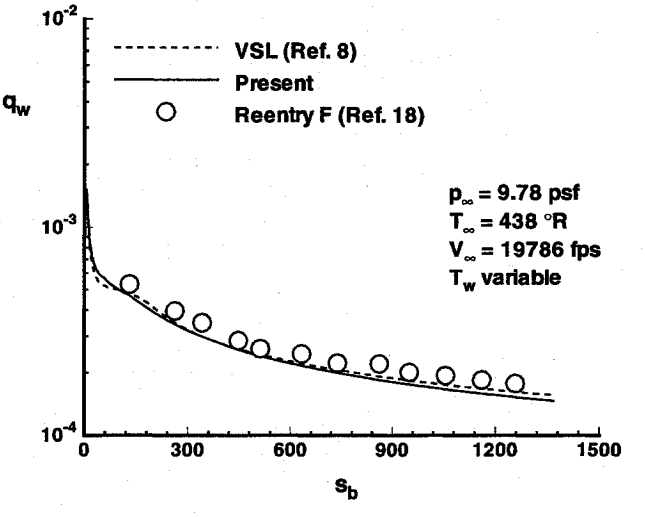

Fig. 7 Heat transfer comparison for 5-deg sphere-cone, R^*_{nose} = .114 in.

pressure distributions (see Fig. 4) are generally in excellent agreement (within 5%), although the differences approach 10% in the pressure overexpansion / recompression region. The surface pressure distribution in the stagnation region is reasonably smooth for all three approaches, so a separate figure highlighting this region is not presented.

The second case features turbulent flow calculations over a long, 5-deg sphere-cone at Mach 15. The nose radius is R^*_{nose} = 1.5 in. and the solution is computed for a body length of $s_{b_{end}}$ = 1125. The freestream conditions are p^*_∞ = 0.01892 psi and T^*_∞ = 478°R, with a wall temperature of T^*_w = 2260°R. The VSL[8] results are published in Ref. 26. Computed surface heating and pressure comparisons are shown in Figs. 5 and 6. The transition point is an input whose value is s_b = 192. From the heating rate comparisons in Fig. 5, both approximate techniques overpredict the VSL results downstream of the nose region (for s_b between approximately 10–100). It is believed that the approximations in Maslen's pressure relation are the source of this deviation. In the overexpansion region, the shock and body angles are quite different for this slender cone (which is inconsistent with Maslen's assumption of a thin shock layer). Apparently, this poor pressure prediction feeds back into the shock shape which is generated as part of the solution. As a result, the calculated shock layer is thinner than that of the VSL solution. Since the thickness gradient plays a prominent role in the governing equations, this deviation is reflected in the shock layer profiles (see Ref. 13), as well as the surface properties. As seen in Fig. 6, both Maslen-based methods compute a reduced overexpansion effect (followed by a smaller recompression) as compared with the VSL solution. The differences between the solutions in the overexpansion / recompression region are approximately 15%. The effect of the differences in this region diminishes further downstream, as can be seen in both figures. A similar phenomena has been seen in the inviscid technique of Riley and DeJarnette,[25] which also employs Maslen's pressure relation. As a final comment, the transition heating results of Grantz et al.[10] reflect an error in the application of the transition model.

Equilibrium

For equilibrium flow, comparisons are made with the Reentry F flight experiment[18] and VSL calculations.[8] Both numerical solutions are generated using Hansen's equilibrium air model.[21] The geometry is a 5-deg sphere-cone with a nose radius of R^*_{nose} = .114 in. and a body length of $s_{b_{end}}$ = 1365. The freestream conditions are p^*_∞ = 0.06792 psi and T^*_∞ = 438°R, with a variable wall temperature. Figure 7 shows that the two calcu-

lated solutions are within 5–10% of each other, although they are both 10–15% below the experimental data.

The second case is flow over a 35.5-deg hyperboloid. The nose radius is $R_{nose} \approx 3.5$ ft and the solution is computed for a body length of $s_{b_{end}} = 24.5$. The freestream conditions are $p_\infty^* = 0.00094$ psi and $T_\infty^* = 400$°R, with a wall temperature of $T_w^* = 1998$°R. Comparisons between the VSL[8] and the current methods are made. Figures 8 and 9 display excellent agreement (within 5%) between the two approaches for surface heating and pressures, respectively. This improved agreement could be due to the large body angle, so that $\Gamma_s \approx \Gamma_b$ everywhere (which more closely matches Maslen's assumptions).

Nonequilibrium

For the first case, calculations are performed for the Mach 25 flow over a 6-deg sphere-cone. The nose radius is $R_{nose}^* = 1.5$ in. and the solution is computed for a body length of $s_{b_{end}} = 250$. The freestream conditions are $p_\infty^* = 0.00794$ psi and $T_\infty^* = 486$°R, with a wall temperature of $T_w^* = 2260$°R. Solutions are generated for both a noncatalytic and fully catalytic wall condition. Computed heating rates are given in Fig. 10. The results of the present and VSL methods differ by approximately 10–15% within the nose region (s_b less than approximately 50). As before, the effect of the differences in the overexpansion / recompression region diminishes further downstream (see Fig. 10), where agreement between the approaches is generally

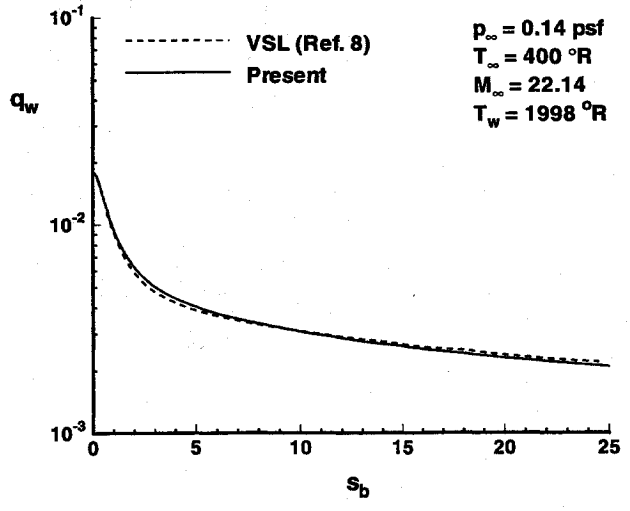

Fig. 8 Heat transfer comparison for 35.5-deg hyperboloid, $R_{nose}^* = 3.46457$ ft.

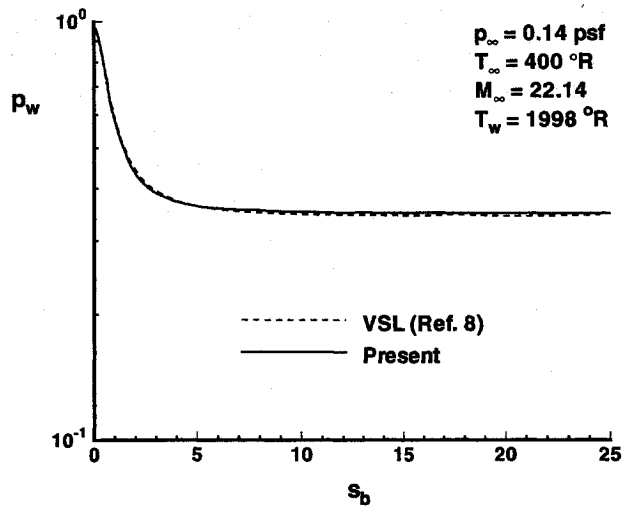

Fig. 9 Body pressure comparison for 35.5-deg hyperboloid, $R_{nose}^* = 3.46457$ ft.

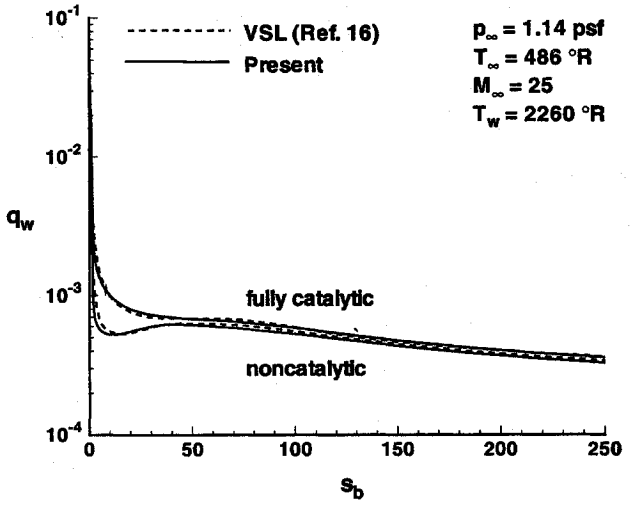

Fig. 10 Heat transfer comparison for 6-deg sphere-cone, $R_{nose}^* = 1.5$ in.

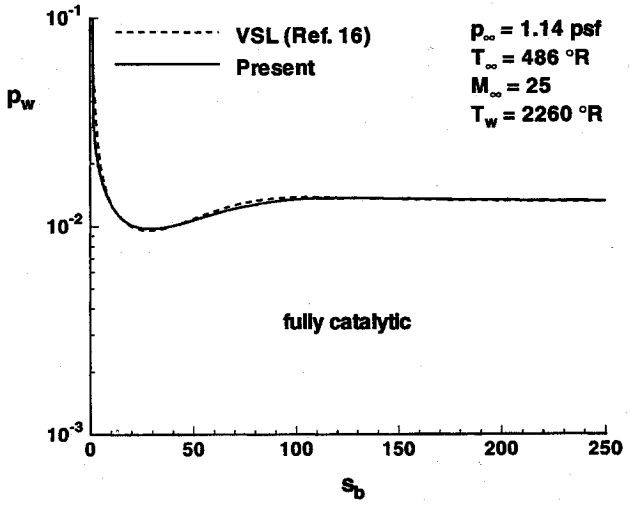

Fig. 11 Body pressure comparison for 6-deg sphere-cone, $R_{nose}^* = 1.5$ in.

within 5%. The catalytic boundary condition has little effect on the pressure, so only the fully catalytic results for the body pressure distribution are presented in Fig. 11. Within the overexpansion / recompression region, the difference between the two solutions is approximately 5%. This is dramatically better than the perfect gas solution over the 5-deg cone presented earlier. The shock layer is thinner for reacting flow than for perfect gas flow. This makes reacting flow better posed for use of Maslen's relation, and hence the better agreement with VSL results. References 13 and 14 provide a more complete analysis of the flowfield through comparisons of shock layer profiles for various properties (including mass fractions).

As a second case, comparisons between the VSL and current methods are made for Mach 25 flow over a 20-deg sphere-cone ($R_{nose}^* = 1.5$ in.) with the same freestream conditions as the previous case. Figure 12 shows that the approximate and VSL surface heating results are generally within 5% of each other for both wall conditions. In the overexpansion region (which is smaller than that of the previous case since this body is blunter) the differences are approximately 15–20%. Note that in the nose region the effects of wall catalysis are large (more than a 50% difference in heating), while further downstream this difference diminishes (to approximately 20%).

Run Times

The purpose of this research is to develop an approach for use in preliminary design where computational speed is an

Table 3 Run times[a] for 6-deg cone, R^*_{nose} = 1.5 in.

VSL	Present	
stations	46	38
CPU time	759	273
grid pts/s/ shock	3	7
shock iterations	3.0	4.2
grid pts/s/ shock	9	30

[a]Sun Sparcstation 1+.

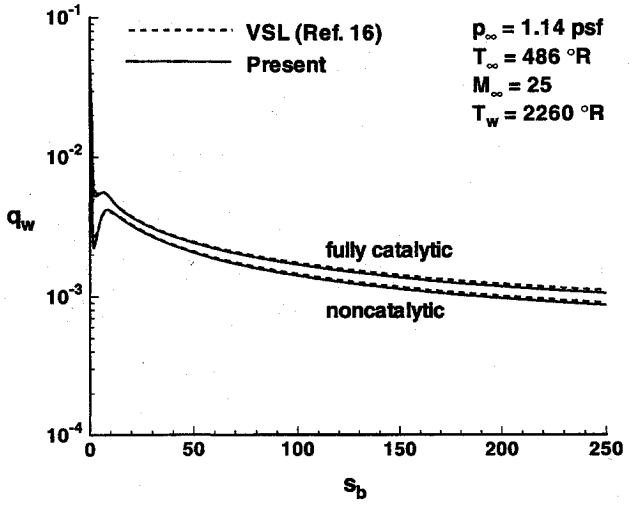

Fig. 12 Heat transfer comparison for 20-deg sphere-cone, R^*_{nose} = 1.5 in.

important consideration. Reference 13 provides a detailed comparison of the run times required by each of the methods to generate these solutions. As an example, Table 3 shows the overall run times required to generate the nonequilibrium solution over the 6-deg cone which was discussed earlier. Since varying numbers of streamwise stations are used by these approaches, the average number of grid points solved per second is also presented. The CPU time shown for the VSL results is the total time required for three global iterations. The present method iteratively determines the shock shape as the solution is advanced from one station to the next. In this case, for a given station, the present technique requires an average of 2.1 iterations to converge the shock shape. The last entry in the table takes into account the number of shock shapes calculated, and gives the processing capabilities of each approach for a given grid and shock shape. For this case, along with others presented in Ref. 13, it is shown that solving the approximate VSL equations of the present method is inherently two to three times as fast as solving the full VSL equations. It should be noted that the method of Ref. 10 is faster still due to its more approximate governing equations.

Conclusions

A new approximate VSL approach to solving hypersonic flowfields about axisymmetric blunt bodies has been developed. The technique, which is self-starting, has been employed for perfect gas, equilibrium, and nonequilibrium flowfields. Using Maslen's pressure relation in lieu of numerically integrating the normal momentum equation is shown to give accurate body pressures (generally within 5% of the VSL values) outside of the pressure overexpansion / recompression region. Within the pressure overexpansion / recompression region, the present method results deviate from the VSL solution. This region of bluntness effects can be large for small cone angles, but diminishes as this angle is increased. Further downstream, as the sharp-cone limit is approached, the present technique shows good agreement with the VSL solution. Excellent agreement between the VSL and approximate heat transfer predictions is seen in the nose region. As a direct result of the stagnation line formulation of the governing equations, the surface properties calculated with the present method approach their stagnation values smoothly. Run time comparisons between the present and VSL techniques show that the present method is inherently two to three times faster than the VSL algorithm. Based on the accuracy of the computed surface properties, this new approach could be useful in the preliminary design environment. Alternately, it could be used to generate starting solutions for more exact methods.

Acknowledgments

This research, supported by Cooperative Agreement NCC1-100, was conducted primarily on-site in the Aerothermodynamics Branch of the Space Systems Division at NASA Langley Research Center, while the first author was a graduate research assistant at North Carolina State University. The authors are indebted to E. Vincent Zoby, the technical monitor, and to the other members of the Aerothermodynamics Branch for their guidance and assistance.

References

[1] Anderson, J. D., Jr., "A Survey of Modern Research in Hypersonic Aerodynamics," AIAA Paper 84-1578, June 1984.

[2] Gnoffo, P. A., "An Upwind-Biased Point-Implicit Relaxation Algorithm for Viscous, Compressible Perfect-Gas Flows," NASA TP 2953, June 1990.

[3] Helliwell, W. S., Dickson, R. P., and Lubard, S. C., "Viscous Flow over Arbitrary Geometries at High Angles of Attack," *AIAA Journal*, Vol. 19, No. 2, 1981, pp. 191–197.

[4] Gnoffo, P. A., "Hypersonic Flows Over Biconics Using a Variable-Effective-Gamma, Parabolized Navier Stokes Code," AIAA Paper 83-1666, July 1983.

[5] Lawrence, S. L., Chaussee, D. S., and Tannehill, J. C., "Application of an Upwind Algorithm to the Three-Dimensional Parabolized Navier-Stokes Equations," AIAA Paper 87-1112, June 1987.

[6] Davis, R. T., "Numerical Solution of the Hypersonic Viscous Shock Layer Equations," *AIAA Journal*, Vol. 8, No. 5, 1970, pp. 843–851.

[7] Moss, J. N., "Reacting Viscous Shock-Layer Solutions with Multicomponent Diffusion and Mass Injection," NASA TR R-411, June 1974.

[8] Murray, A. L., and Lewis, C. H., "Hypersonic Three-Dimensional Viscous Shock Layer Flows over Blunt Bodies," *AIAA Journal*, Vol. 16, No. 12, 1978, pp. 1279–1286.

[9] Gupta, R. N., Gnoffo, P. A., and MacCormack, R. W., "Viscous Shock-Layer Flowfield Analysis by an Explicit-Implicit Method," *AIAA Journal*, Vol. 23, No. 5, 1985, pp. 723–732.

[10] Grantz, A. C., DeJarnette, F. R., and Thompson, R. A., "Approximate Viscous Shock-Layer Method for Hypersonic Flow over Blunt-Nosed Bodies," *Journal of Spacecraft and Rockets*, Vol. 27, No. 6, 1990, pp. 597–605.

[11] Maslen, S. H., "Asymmetric Hypersonic Flow," NASA CR 2133, Sept. 1971.

[12] Cheatwood, F. M., and DeJarnette, F. R., "An Approximate Viscous Shock Layer Approach to Calculating Hypersonic Flows about Blunt-Nosed Bodies," AIAA Paper 91-1348, June 1991.

[13] Cheatwood, F. M., and DeJarnette, F. R., "An Approximate Viscous Shock Layer Technique for Calculating Chemically Reacting Hypersonic Flows about Blunt-Nosed Bodies," NASA CR 187617, Aug. 1991.

[14] Cheatwood, F. M., and DeJarnette, F. R., "An Approximate Viscous Shock Layer Technique for Calculating Nonequilibrium Hypersonic Flows about Blunt-Nosed Bodies," AIAA Paper 92-0498, Jan. 1992.

[15] Gupta, R. N., Lee, K. P., Zoby, E. V., Moss, J. N., and Thompson, R. A., "Hypersonic Viscous Shock-Layer Solutions over Long Slender Bodies—Part I: High Reynolds Number Flows," *Journal of Spacecraft and Rockets*, Vol. 27, No. 2, 1990, pp. 175–184.

[16] Zoby, E. V., Lee, K. P., Gupta, R. N., Thompson, R. A., and Simmonds, A. L., "Viscous Shock-Layer Solutions with Nonequilibrium Chemistry for Hypersonic Flows past Slender Bodies," *Journal of Spacecraft and Rockets*, Vol. 26, No. 4, 1989, pp. 221–228.

[17] Cleary, J. W., "Effects of Angle of Attack and Bluntness on Laminar Heating-Rate Distributions on a 15 Degree Cone at a Mach Number of 10.6," NASA TN 5450, Oct. 1969.

[18] Stainback, P. C., Johnson, C. B., Boney, L. B., and Wicker, K. C., "Comparison of Theoretical Predictions and Heat-Transfer Measurements for a Flight Experiment at Mach 20 (Reentry F)," NASA TM-X 2560, 1972.

[19] Cebeci, T., "Behavior of Turbulent Flow near a Porous Wall with Pressure Gradient," *AIAA Journal,* Vol. 8, No. 12, 1970, pp. 2152–2156.

[20] Blottner, F. G., "Viscous Shock Layer at the Stagnation Point with Nonequilibrium Air Chemistry," *AIAA Journal,* Vol. 7, No. 12, 1969, pp. 2281–2288.

[21] Hansen, C. F., "Approximations for the Thermodynamic and Transport Properties of High Temperature Air," NASA TR R-50, 1959.

[22] Thompson, R. A., Lee, K. P., and Gupta, R. N., "Computer Codes for the Evaluation of Thermodynamic Properties, Transport Properties, and Equilibrium Constants of an 11-Species Air Model," NASA TM 102602, Feb. 1990.

[23] Armaly, B. F., and Sutton, K., "Viscosity of Multicomponent Partially Ionized Gas Mixtures," AIAA Paper 80-1495, July 1980.

[24] Mason, E. A., and Saxena, S. C., "Approximate Formula for the Thermal Conductivity of Gas Mixtures," *Physics of Fluids,* Vol. 3, No. 5, 1958, pp. 361–369.

[25] Riley, C. J., and DeJarnette, F. R., "Engineering Calculations of Three-Dimensional Inviscid Hypersonic Flow Fields," *Journal of Spacecraft and Rockets,* Vol. 28, No. 6, 1991, pp. 628–635.

[26] Thompson, R. A., Zoby, E. V., Wurster, K. E., and Gnoffo, P. A., "An Aerothermodynamic Study of Slender Conical Vehicles," AIAA Paper 87-1475, June 1987.